J. Fluid Mech. (2010), *vol.* 654, *pp.* 387–416.
doi:10.1017/S0022112010000649

DNS of the thermal effects of laser energy deposition in isotropic turbulence

SHANKAR GHOSH AND KRISHNAN MAHESH†

Aerospace Engineering and Mechanics, University of Minnesota, MN 55455, USA

(Received 4 November 2008; revised 1 February 2010; accepted 1 February 2010; first published online 14 May 2010)

The interaction of a laser-induced plasma with isotropic turbulence is studied using numerical simulations. The simulations use air as the working fluid and assume local thermodynamic equilibrium. The numerical method is fully spectral and uses a shock-capturing scheme in a corrector step. A model problem involving the effect of energy deposition on an isolated vortex is studied as a first step towards plasma/turbulence interaction. Turbulent Reynolds number $Re_\lambda = 30$ and fluctuation Mach numbers $M_t = 0.001$ and 0.3 are considered. A tear-drop-shaped shock wave is observed to propagate into the background, and progressively become spherical in time. The turbulence experiences strong compression due to the shock wave and strong expansion in the core. This behaviour is spatially inhomogeneous and non-stationary in time. Statistics are computed as functions of radial distance from the plasma axis and angular distance across the surface of the shock wave. For $M_t = 0.001$, the shock wave propagates on a much faster time scale compared to the turbulence evolution. At M_t of 0.3, the time scale of the shock wave is comparable to that of the background. For both cases the mean flow is classified into shock formation, shock propagation and subsequent collapse of the plasma core, and the effect of turbulence on each of these phases is studied in detail. The effect of mean vorticity production on the turbulent vorticity field is also discussed. Turbulent kinetic energy budgets are presented to explain the mechanism underlying the transfer of energy between the mean flow and background turbulence.

1. Introduction

A laser-induced plasma is produced by focusing a pulsed laser beam onto a small volume of a gas. When the electric field of the laser radiation near the focal volume exceeds the field binding the electrons to their respective nuclei, it triggers breakdown of the gas molecules and ionizes the gas in the focal volume. The resulting plasma is opaque to the incident laser radiation and absorbs more energy, resulting in further ionization. This generates a cascade effect. Energy is preferentially absorbed towards the laser source, and hence an elongated tear-drop-shaped spark is produced at the end of the laser pulse. The collision of energetic electrons with heavy particles heats the gas. The resulting de-energized electrons recombine with heavy particles, and the electron number density decreases as a result. Very high temperatures and pressures are obtained at the end of plasma formation. The resulting pressure gradients cause a blast wave which then propagates into the background gas. As the blast wave propagates into the background, it poses an interesting fluid dynamic problem. The

† Email address for correspondence: mahesh@aem.umn.edu

blast wave is initially tear drop shaped but becomes spherical as it propagates. During this period, the strength of the blast wave varies over two orders of magnitude. The flow field behind the blast wave results in rolling up of the plasma core, and formation of toroidal vortex rings.

Laser-induced breakdown has a variety of applications, the most popular probably being laser-induced breakdown spectroscopy (LIBS). Laser-induced breakdown spectroscopy is a type of atomic emission spectroscopy that uses a highly energetic laser pulse as the excitation source. Recently, laser-induced breakdown has been considered for various aerospace-related applications. These involve the control of supersonic flows (Adelgren *et al.* 2003), drag reduction in supersonic and hypersonic flows (Riggins, Nelson & Johnson 1999) and provision of thrust to aerospace vehicles (Molina-Morales *et al.* 2001; Wang *et al.* 2001). Most of these applications consider generation of a laser-induced plasma in steady flows. However, most flows of practical importance are turbulent in nature. Little or no work has been undertaken so far in studying the interaction of a laser-induced plasma with a turbulent flow. A laser-induced plasma provides an ideal means for localized energy deposition in a turbulent flow; it allows precise control over the amount of energy deposited and the location and timing of energy deposition. The mutual interaction between the turbulence and features such as the blast wave, the high-temperature core and the toroidal vortex ring poses a very interesting problem. The parameters relevant to the problem are magnitude of energy deposited, Reynolds number, fluctuation Mach number and length scale of the turbulence compared to the spark size.

When laser-induced breakdown occurs in isotropic turbulence, the resulting blast wave interacts with the turbulent field. Such shock/turbulence interactions have been studied by many researchers. Jacquin, Blin & Geffroy (1993) generated grid turbulence in accelerated flows up to a Mach number of 1.4 and found the turbulence amplification across the shock wave to be low. Agui (1998) obtained data that suggests an amplification of the longitudinal velocity fluctuations, whereas the fluctuations of the other two components are slightly decreased or remain unchanged through the interactions. Numerical simulations and linear analysis of the interaction have been performed and much of the physical processes behind the interaction explained. Much of this work is reviewed by Lee, Lele & Moin (1993, 1997) and Mahesh, Lele & Moin (1994, 1995, 1997). However, in the context of laser-induced breakdown, the shock wave is not plane and of constant strength. Instead, it is initially tear drop shaped and later evolves to become spherical. Its strength increases initially when it forms and decreases later when it propagates. The shock strength is not constant across the shock front. Turbulence at different distances from the plasma core would therefore interact with shock waves of different strengths; after the shock wave passes, it leaves behind very inhomogeneous turbulence which then interacts with the plasma core. In statistical terms, the turbulence is non-stationary and inhomogeneous along the spark axis and radial directions.

Our past work (Ghosh & Mahesh 2008) has studied laminar laser-induced breakdown in quiescent air. The processes of shock formation, propagation and subsequent collapse of the plasma core to form a toroidal vortex ring were examined. Vorticity generation in the flow was described for short and long times. Scaling analysis was performed for different amounts of laser energy deposited and different Reynolds number of the flow. Also, the simulations were performed using three different models for air and the impact of these models on the flow field was discussed.

This paper studies laser energy deposition in isotropic turbulence. A schematic view for the resulting flow field is shown in figure 1. Figure 1(*a*) shows laser-induced

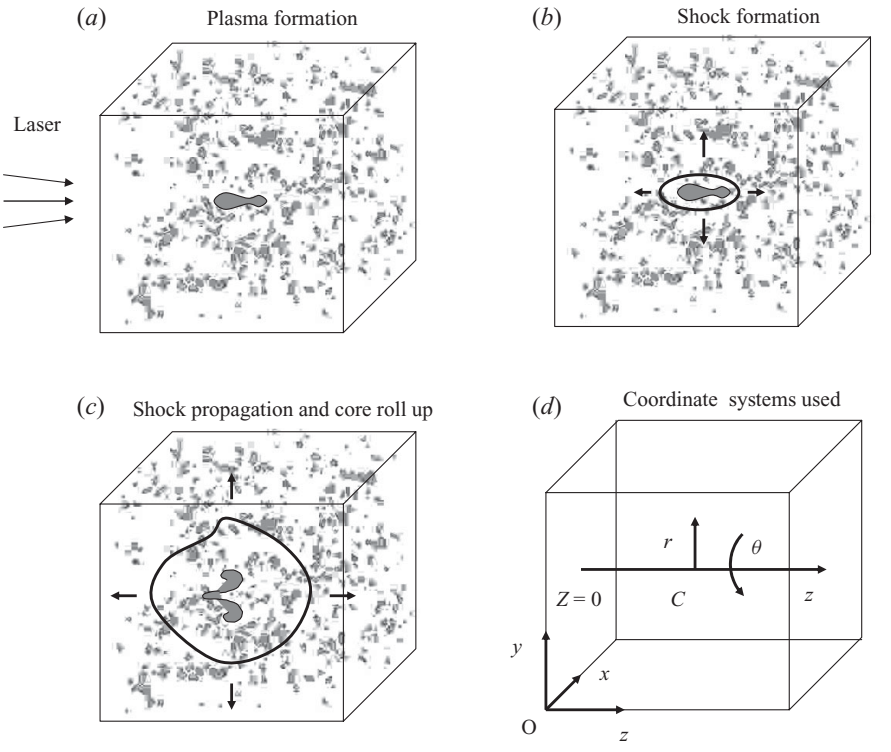

FIGURE 1. Schematic showing (*a*) laser-induced plasma formation in isotropic turbulence, (*b*) shock formation in isotropic turbulence, (*c*) propagation of the shock wave through the background turbulence and roll up of the plasma core, (*d*) coordinate systems used.

plasma formation in isotropic turbulence. The laser beam is focused from left to right. Figure 1(*b*) shows formation of a tear-drop-shaped shock wave and figure 1(*c*) shows propagation of this shock wave through the background turbulence and rolling up of the plasma core in time producing vorticity. Figure 1(*d*) shows the different coordinate systems used in this work to obtain and interpret the simulation results. The flow field is simulated using a three-dimensional Cartesian coordinate system with origin at point *O*. Since the resulting mean flow is axisymmetric, the turbulent statistics are obtained using an axisymmetric coordinate system passing through *C*, the centre of the flow domain. Note that $z = 0$ for this coordinate system coincides with that of the Cartesian coordinate system.

A model problem involving the effect of energy deposition on a single vortex is studied as a first step. Budgets are computed for the laminar vorticity transport equation and the results are used to explain laser energy deposition in isotropic turbulence. For the turbulent problem, $Re_\lambda = 30$ and fluctuation Mach numbers $M_t = 0.001$ and 0.3 are considered for the background turbulence. M_t of 0.001 is chosen to correspond to low-speed experiments (e.g. Comte-Bellot & Corrsin 1971). Here, the shock wave propagates on a much faster time scale compared to the turbulence evolution. The turbulence ahead of the shock is therefore almost frozen. At M_t of 0.3 the time scales of the shock wave are comparable to that of the background. The effect of the turbulence on shock formation, propagation and roll up is studied for both cases. Suppression of mean core roll up for the $M_t = 0.3$ case is explored based on energy of the mean flow and mean shock shape.

A significant effect of the mean flow on the background turbulence is observed for both $M_t = 0.001$ and 0.3 cases. The turbulence experiences strong compression due to the shock wave and strong expansion in the core. Turbulence intensities are enhanced and suppressed due to the effects of compression and expansion, respectively. This behaviour is spatially inhomogeneous and non-stationary in time. Effect on the turbulence is studied by computing statistics for different flow variables. Also, the effect of mean vorticity production on the turbulent vorticity field is discussed. Budgets are computed for different terms on the right-hand side of the turbulent kinetic energy equation and are used in combination with the mean kinetic energy equation to understand the mechanism of energy transfer between the mean flow and the turbulent background.

The paper is organized as follows. Section 2 describes the simulation methodology. Section 2.1 provides a description of the algorithm used and the primary numerical challenges posed by the flow. Section 2.2 contains validation results for the algorithm. Section 3 presents simulation results for energy deposition near an isolated vortex. Simulation results for laser energy deposition are presented in § 4. Section 4.1 describes the flow field in absence of turbulence. Effects of the turbulent fluctuations on the mean flow are discussed in § 4.2. Sections 4.2.1, 4.2.2 and 4.2.3 describe the effects on shock formation, shock propagation and roll up in the mean. The effects of the mean flow on the turbulent fluctuations are described in § 4.3. Section 4.3.1 describes the method for computation of the turbulent statistics. Section 4.3.2 presents results for $M_t = 0.001$ and § 4.3.3 presents results for $M_t = 0.3$. Section 4.4 discusses the effects of mean vorticity production on the vorticity fluctuations. Turbulent kinetic energy budgets are presented in § 4.5. A short summary in § 5 concludes the paper.

2. Simulation methodology

2.1. *Algorithm description*

The flow field resulting from laser-induced breakdown in isotropic turbulence is simulated using the compressible Navier–Stokes equations. Details of the numerical method are presented in Ghosh & Mahesh (2008). Local thermodynamic equilibrium conditions are assumed to be applicable. Radiation losses from the hot plasma core are assumed to be negligible. Under these assumptions, the equations for the conservation of mass, momentum and energy can be written as

$$\frac{\partial \rho}{\partial t} + \frac{\partial \rho u_i}{\partial x_i} = 0, \tag{2.1}$$

$$\frac{\partial \rho u_j}{\partial t} + \frac{\partial \rho u_j u_i}{\partial x_i} = -\frac{\partial}{\partial x_i}\left[p\delta_{ij} - \frac{\mu}{Re}\left(\frac{\partial u_i}{\partial x_j} + \frac{\partial u_j}{\partial x_i} - \frac{2}{3}\frac{\partial u_k}{\partial x_k}\delta_{ij}\right)\right], \tag{2.2}$$

$$\frac{\partial \rho e_T}{\partial t} + \frac{\partial \rho e_T u_i}{\partial x_i} = \frac{\partial}{\partial x_i}\left[-pu_i + \frac{\mu}{Re}\left(\frac{\partial u_i}{\partial x_j} + \frac{\partial u_j}{\partial x_i} - \frac{2}{3}\frac{\partial u_k}{\partial x_k}\delta_{ij}\right)u_j\right] + \frac{\partial}{\partial x_i}\left(\frac{\kappa}{(\gamma-1)RePr}\frac{\partial T}{\partial x_i}\right). \tag{2.3}$$

All variables are non-dimensionalized with respect to their background initial values:

$$\begin{gathered} x_i = x_i^*/L_0^*, \quad u_i = u_i^*/c_0^*, \quad t = t^* c_0^*/L_0^*, \\ \rho = \rho^*/\rho_0^*, \quad p = p^*/\rho_0^* c_0^{*2}, \quad T = T^*/T_0^*, \\ \mu = \mu^*/\mu_0^*, \quad \kappa = \kappa^*/\kappa_0^*. \end{gathered} \tag{2.4}$$

Here, the subscript 0 denotes initial background values and the superscript * denotes dimensional variables. L_0^* is the reference length scale and c_0^* is the speed of sound based on initial background temperature, i.e.

$$c_0{}^* = (\gamma R^* T_0{}^*)^{1/2}. \tag{2.5}$$

The Reynolds number and Prandtl number are defined as

$$Re = \rho_0{}^* c_0{}^* L_0{}^* / \mu_0{}^*, \quad Pr = \mu^* c_p{}^* / k^*. \tag{2.6}$$

Simulating laser-induced breakdown involves very high temperatures. At these temperatures the background air undergoes ionization, dissociation, recombination, charge exchange, charge transfer and Zeldovich reactions. These result in formation of a multi-species plasma. At equilibrium, the number of species present in significant quantity at any given time and their concentration depends upon the temperature and pressure of the plasma. The simulations consider an 11 species model for air. These species are

$$N_2,\ O_2,\ NO,\ N,\ O,\ N_2{}^+,\ O_2{}^+,\ NO^+,\ N^+,\ O^+ \text{ and } e^-.$$

The thermodynamic and transport properties of air are then obtained as functions of temperature and pressure. The Navier–Stokes equations are then solved using these properties. This model ignores thermal, chemical and radiational non-equilibrium effects which are important during plasma formation. However, as shown in § 4.1, all experimentally observed gas-dynamic aspects of the flow field are successfully reproduced.

The governing equations are solved using Fourier methods to compute the spatial derivatives. A colocated approach is used and the solution is advanced in time using a fourth-order Runge–Kutta scheme. A skew-symmetric representation is used for all non-linear terms to suppress aliasing error. The above algorithm is implemented for parallel platforms using message passing interface (MPI). The solver assumes periodic boundary conditions. The flow resulting from laser energy deposition is axisymmetric and non-stationary in time. The effects of periodic boundary conditions are not insignificant, especially at later times. However, as long as the laser energy deposition region and its effect on the background turbulence stays far from the domain boundaries, the effects of the periodic boundary conditions are small.

Simulating laser-induced breakdown in a turbulent background poses a number of numerical challenges. Recall that localized laser energy deposition results in propagation of a strong shock wave through the domain. Since the flow solver uses spectral methods for spatial discretization, resolving these sharp gradients requires a highly refined mesh. The Fourier spectral method is therefore combined with a shock-capturing scheme proposed by Yee, Sandham & Djomehri (1999), to reduce computational cost. The shock-capturing scheme is based on the finite-volume methodology, and is applied as a corrector step to the Fourier discretization used in this paper. In the first step, the predicted form of the solution vector is obtained using Fourier methods. This solution vector is then corrected using the numerical fluxes obtained from a characteristic based filter. The approach by Yee *et al.* (1999) is extended to the high-temperature equations in order to remain consistent with the predictor step.

The base shock-capturing scheme due to Yee *et al.* (1999) is found to dissipate the background turbulence excessively. Therefore, for accurate simulation of the background turbulence a nonlinear limiter (Ducros *et al.* 1999), which turns on the shock capturing only in the vicinity of the shock wave, is used. The limiter is

given by

$$g = \frac{\theta^2}{\theta^2 + \omega^2}, \tag{2.7}$$

where θ denotes divergence of velocity and ω denotes vorticity magnitude. Note that g is small in regions where $\theta \ll \omega$ and is close to 1 where $\theta \gg \omega$. Hence, this limiter can be used to limit the application of the corrective numerical fluxes only in the vicinity of the shock wave, thus avoiding dissipation of the entire turbulent field. The limiter is used as a multiplier to the corrective numerical fluxes obtained from the shock-capturing scheme. Also, to prevent the limiter from getting activated in expansion regions near the core, the value of g is set to zero for any $\theta > 0$.

Another numerical difficulty is caused by the presence of very low density in the plasma core. When laser energy is added to a flow at rest, there is noticeable expansion of the core. This results in very small values of density in the core. When the continuity equation was advanced in time with density as the dependent variable, the solution was found to become unstable. It was therefore decided to solve for the logarithm of density as the variable. Define

$$v = \ln \rho \qquad \Rightarrow \qquad \rho = \mathrm{e}^v. \tag{2.8}$$

The continuity equation becomes

$$\frac{\partial v}{\partial t} + u_i \frac{\partial v}{\partial x_i} = -\frac{\partial u_i}{\partial x_i}. \tag{2.9}$$

Note that ρ is always positive when computed as e^v, even for very small values of ρ. The $\log \rho$ formulation of the continuity equation therefore makes the solution stable in regions of very low density.

2.2. *Validation results*

To validate the accuracy of the algorithm, a number of test simulations are performed. Decaying isotropic turbulence is simulated corresponding to the direct numerical simulation (DNS) of Blaisdell, Mansour & Reynolds (1991). The initial M_t used is 0.3 and Re_λ used is 28.5. A top-hat initial energy spectrum with energy in wavenumbers 8 to 16 is used and the simulations are conducted on a 128 cube mesh. Time evolution of Re_λ and the dissipation rate are compared to data from Blaisdell and his colleagues (figures 2*a* and 2*b*) and are found to agree very well.

Accuracy of the shock-capturing scheme in a turbulent background and effectiveness of the Ducros limiter are tested by simulating decaying isotropic turbulence for three different cases. For the first case, no shock capturing is used. For the second case, shock capturing is used without the Ducros limiter and for the third case, shock capturing is used along with the Ducros limiter. For all three cases, the initial $M_t = 0.3$ and $Re_\lambda = 50$. A power four initial energy spectrum peaking at wavenumber 5 is used and all simulations are conducted on a 128 cube mesh. Figure 3 shows decay of turbulent kinetic energy in time for all three simulations. It is observed that the added dissipation from the shock-capturing results in underprediction of the turbulent kinetic energy. Use of the Ducros limiter removes this excessive dissipation by turning off shock capturing in absence of a shock wave.

Activation of the Ducros limiter only in the vicinity of the shock wave is demonstrated using laser energy deposition in isotropic turbulence. The simulation conditions are stated in § 4 ($M_t = 0.001$ case). Laser energy deposition results in the formation of a tear-drop-shaped shock wave that becomes spherical in time (§ 4.1). Figure 4 shows contours of the Ducros variable g (defined in (2.7)) at different instants

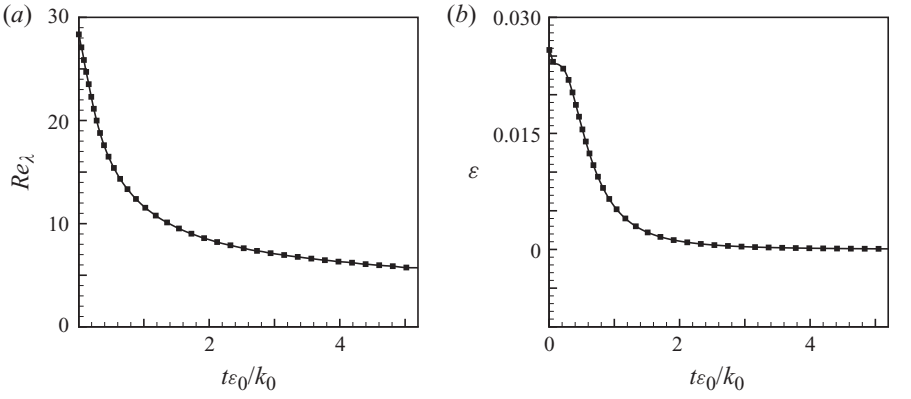

FIGURE 2. Comparison to Blaisdell (1991), time evolution of (*a*) Re_λ and (*b*) ε, ——— simulation results, ■ Blaisdell's data, ε_0 and k_0 denote the initial total dissipation rate and the initial turbulent kinetic energy, respectively.

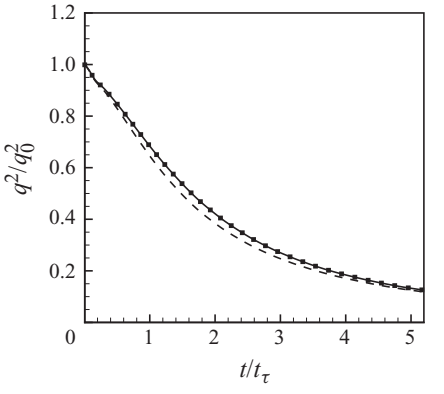

FIGURE 3. Validation of the Ducros limiter, turbulent kinetic energy decay in time, ——— without shock capturing, – – – – with shock capturing, ■ with shock-capturing and nonlinear limiter, t_τ denotes the eddy turn over time scale.

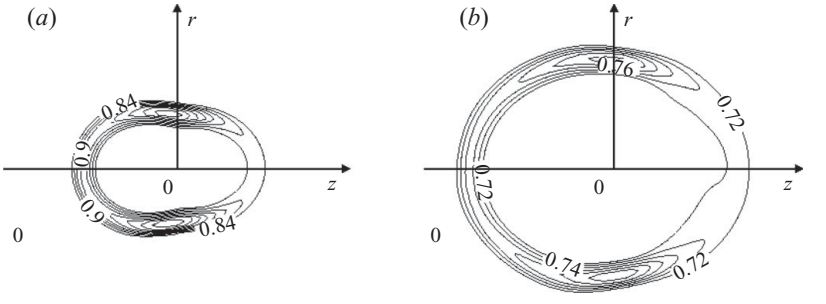

FIGURE 4. Contours of the Ducros variable g at $t = 0.45$ (*a*) and 0.9 (*b*) showing activation of the limiter only in the vicinity of the shock wave.

of time. Note that the limiter gets activated only in a localized region in the vicinity of the shock wave and the contours of g also show the formation of a tear-drop-shaped shock wave becoming spherical in time. Also, the value of g lies between 0 and 1 and its magnitude decreases with decreasing strength of the shock wave in time.

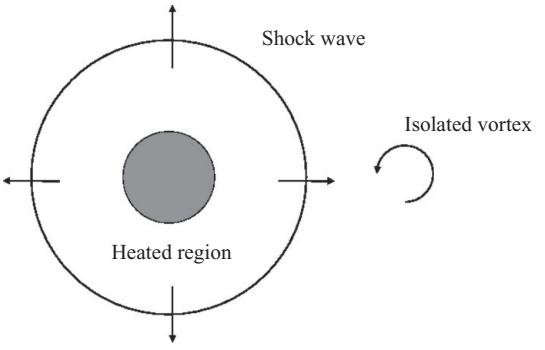

FIGURE 5. Schematic showing interaction of an energy deposition region with an isolated vortex in two dimensions.

3. Effect of energy deposition on an isolated vortex

In this section, interaction of an energy deposition region with an isolated vortex is studied as a first step towards plasma–turbulence interaction. A two-dimensional problem is studied for the sake of simplicity. A schematic view of the problem is shown in figure 5. A circular region is heated at the centre of the domain resulting in formation of a circular shock wave. This shock wave propagates into the background interacting with the isolated vortex located at a certain distance from the centre of the heated region. The length of the domain is 2π in each direction and a 320 point computational mesh is used for the simulation. The ratio of the maximum initial temperature at the centre of the heated region to that of the background temperature is 30 and initial maximum vorticity at the centre of the vortex region is 1.57. The initial distance between the centre of the heated region and that of the vortex is 1.4π. Computational Reynolds number used for the simulation is 200.

The propagating shock wave compresses the vortex. Since the shock strength changes in time, the extent of compression experienced by the vortex also changes with time. Behind the shock wave, the vortex experiences expansion due to the expanding core of the heated region. The extent of expansion experienced by the vortex is also time-dependent. Figure 6 shows evolution of the flow field at three different instants of time using contours of vorticity, velocity magnitude and pressure. The first time instant corresponds to the initial flow field. Initial locations of the thermal region and the isolated vortex are shown by contours of pressure and vorticity, respectively. The second time instant corresponds to maximum compression of the vortex when the shock front lies directly over it. At the third instant of time, the vortex experiences expansion due to the effect of the expanding core. The extent to which the vortex structure gets distorted as result of interaction with the shock wave can be observed from the velocity contours. Both velocity and pressure contours show that the shock front also gets significantly distorted in the interaction. The vorticity contours show that the vortex gets compressed in the direction of shock propagation. Also, the vortex is found to advect along the direction of shock propagation. Since the advection velocity is smaller than the shock velocity, the vortex is exposed to the expanding core behind the shock front at longer times.

Fluid properties are obtained in time following the centre of the vortex. Figures 7(a) and 7(b) show that when the vortex experiences compression its vorticity increases, while when it experiences expansion its vorticity decreases. Note that the instant of time when the vorticity starts decreasing corresponds to the instant when the

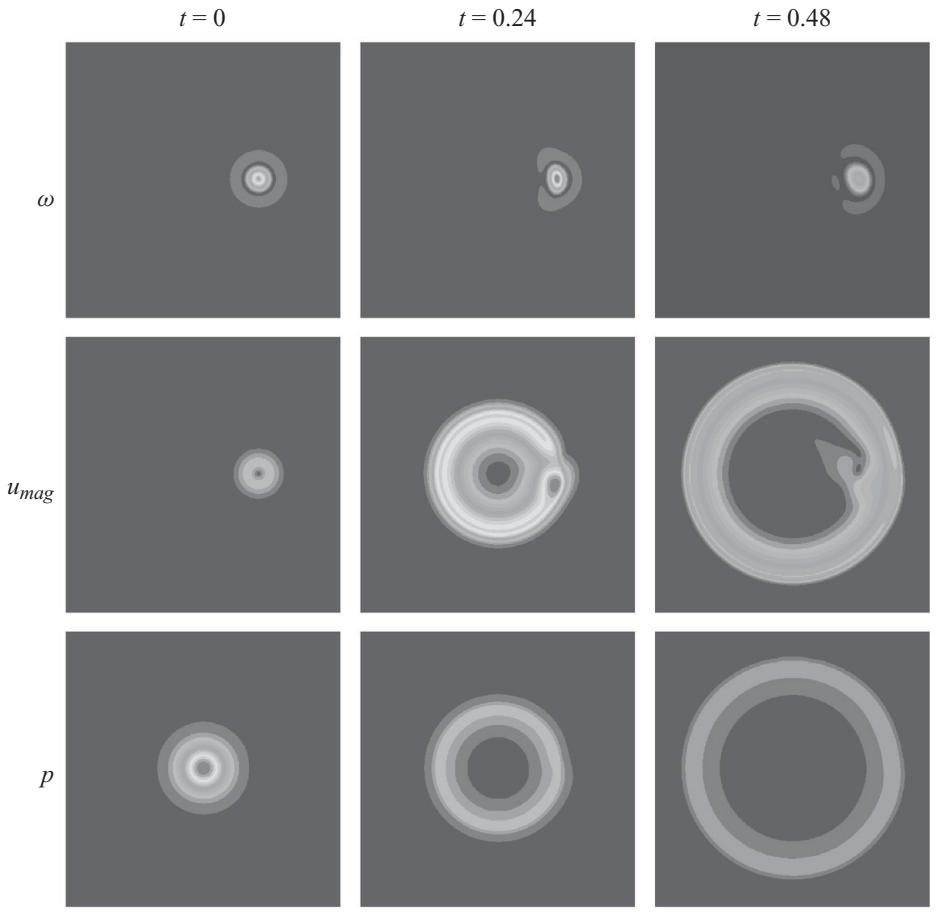

FIGURE 6. Contours of vorticity, velocity magnitude and pressure at $t = 0$, 0.24 and 0.48.

vortex centre begins to get influenced by the expanding core. The amplification and suppression of vorticity levels can be explained based on budgets for the vorticity equation:

$$\frac{\partial \boldsymbol{\omega}}{\partial t} = \underbrace{-(\boldsymbol{u}\cdot\nabla)\boldsymbol{\omega}}_{\text{Advection}} + \underbrace{(\boldsymbol{\omega}\cdot\nabla)\boldsymbol{u}}_{\text{Vortex stretching/tilting}} - \underbrace{\boldsymbol{\omega}(\nabla\cdot\boldsymbol{u})}_{\text{Bulk dilatation}} - \underbrace{\frac{\nabla p\times\nabla\rho}{\rho^2}}_{\text{Baroclinic}} + \frac{1}{Re}\underbrace{\left(\nabla\times\left(\frac{1}{\rho}\nabla\cdot\boldsymbol{\tau}\right)\right)}_{\text{Viscous}}. \quad (3.1)$$

Budgets are computed for the different terms on the right-hand side of (3.1). These budgets are obtained as a function of time at the centre of the vortex and are shown in figure 7(*c*). The bulk dilatation and viscous terms are found to dominate. The bulk dilatation term is positive initially and helps enhance the vorticity levels. Later, as the centre of the vortex is exposed to expansion, the bulk dilatation term becomes negative and causes a decrease in the vorticity levels. The viscous term is always negative leading to the decrease of vorticity at all times. However its effect is

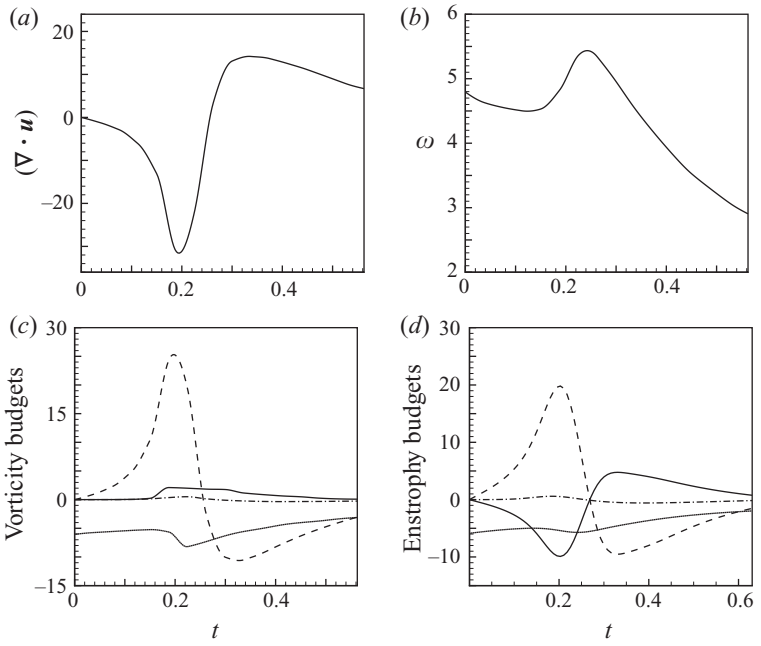

FIGURE 7. (*a*, *b*) Velocity divergence and vorticity at the vortex centre; (*c*, *d*) vorticity budgets at the vortex centre and integrated enstrophy budgets; ——— : advection term, – – – – : bulk dilatation term, —·— : baroclinic term and ····· : viscous term.

maximum when the vortex centre faces maximum compression. This is because the compression results in larger velocity gradients, thus enhancing the shear stresses at the vortex centre. The advection term is small due to small gradients in vorticity at the vortex centre. The baroclinic term is much smaller compared to the other terms. Since the problem is two-dimensional, the vortex stretching/tilting term is zero.

Integrated enstrophy budgets are computed similar to Erlebacher & Hussaini (1998) to study the global evolution of the flow. The enstrophy transport equation can be obtained by taking an inner product of (3.1) with $\boldsymbol{\omega}$. Budgets are shown (figure 7*d*) for different terms on the right-hand side of the enstrophy transport equation integrated over the entire domain and normalized with integrated initial enstrophy. The advection term is found to be comparable in magnitude to the bulk dilatation and viscous terms. Evolution of all other terms is similar to that observed for the single-point budgets shown at the centre of the vortex (figure 7*c*).

Note that this problem is different from the classical problem of a vortex interacting with a stationary shock wave. Firstly, as the shock wave interacts with the vortex its strength changes in time. Secondly, the vortex experiences a change from compression to expansion as the shock wave passes through it. Thirdly, the vortex gets advected in the direction of the shock wave. These distinct features make this problem an appropriate simplification for studying interaction of a laser-induced plasma with isotropic turbulence.

4. Laser-induced plasma simulations

This section contains simulation results for laser energy deposition. Energy deposition is described both in quiescent air and in isotropic turbulence. While

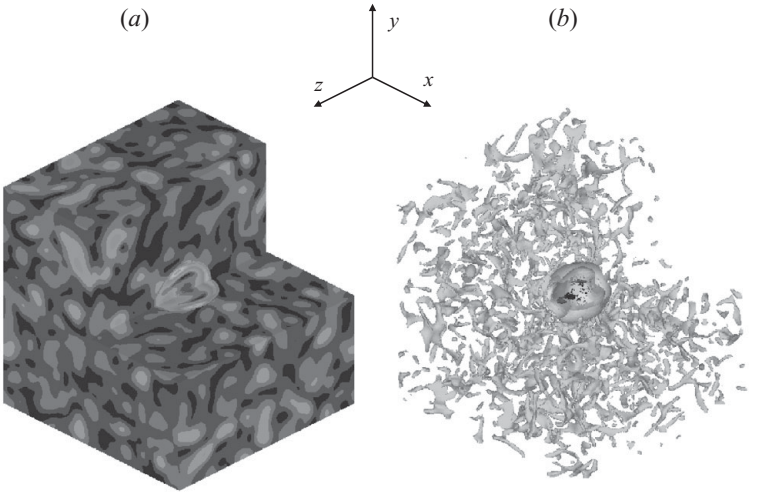

FIGURE 8. Three-dimensional visualization of the flow field resulting from laser energy deposition in isotropic turbulence: (*a*) velocity magnitude contours and (*b*) isocontours of density plotted over isocontours of vorticity.

only a brief description of the laminar simulation is provided, the turbulent problem is studied in detail. All simulations are conducted on a cubic structured mesh. Each dimension of the cube contains 320 grid points over a domain length of 2π.

A three-dimensional view of the flow field resulting from laser energy deposition in isotropic turbulence is shown in figure 8. Figure 8(*a*) shows contours of velocity magnitude while figure 8(*b*) shows isocontours of density plotted over isocontours of vorticity at the same instant of time. A slice containing the top right quarter of the cube is removed from both figures to provide an inner view of the flow field. The density isocontours show location of the shock front and the vorticity isocontours show turbulence in the background. A tear-drop-shaped shock wave is observed to propagate into the background. Heavy interaction between the shock wave, the high energy core and the background turbulence is observed. The effect of turbulence on the mean flow and the effect of mean flow on the turbulence are both studied in detail.

The turbulent initial conditions are generated using Rogallo's method (Rogallo 1981). The initial velocity fluctuations are isotropic and divergence free, while initial fluctuations in pressure, temperature and density are assumed to be zero. The initial energy spectrum used in the simulations is a power four spectrum peaking at wavenumber $k_0 = 5$

Let $u_{rms} = \bar{u'^2}$ be the root mean square (r.m.s.) velocity along the x direction. The turbulent kinetic energy is given by

$$q^2 = \bar{u'^2} + \bar{v'^2} + \bar{w'^2}, \tag{4.1}$$

where u', v' and w' are velocity fluctuations along the x, y and z directions, respectively. Then $q = \sqrt{3}u_{rms}$. Define fluctuation Mach number M_t as

$$M_t = \frac{q}{c_0}, \tag{4.2}$$

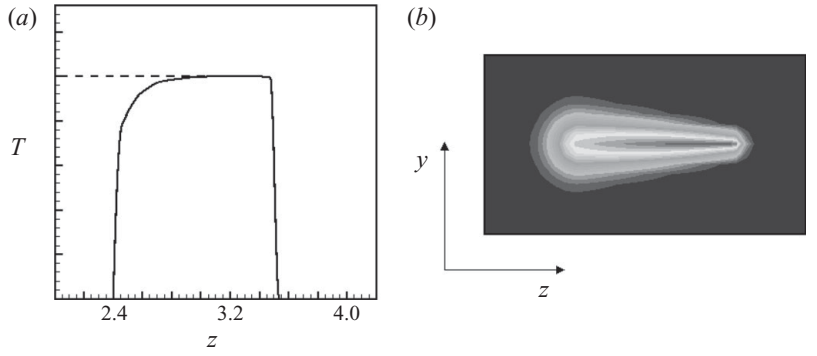

FIGURE 9. (*a*) Axial variation of the initial mean temperature profile, (*b*) Contours of initial mean temperature in a plane through the plasma axis.

where $c_0 = 1$ is the non-dimensional speed of sound. Then, $M_t = \sqrt{3}u_{rms}$. The turbulent Reynolds number Re_λ is given by

$$Re_\lambda = \frac{\lambda^* {u_{rms}}^* \rho^*}{\mu^*}, \tag{4.3}$$

where λ^* is the dimensional Taylor microscale. Upon non-dimensionalizing using (2.4), Re_λ is obtained as

$$Re_\lambda = Re\lambda \frac{\rho}{\mu} \frac{M_t}{\sqrt{3}}, \tag{4.4}$$

where the Reynolds number Re is defined in § 2 and $\lambda = 0.4$ for a power four initial energy spectrum peaking at wavenumber $k_0 = 5$. Simulations are conducted for $Re_\lambda = 30$ and $M_t = 0.001$ and 0.3.

The initial turbulent flow is allowed to evolve until the velocity derivative skewness assumes a steady value between -0.4 and -0.5. The effect of initial conditions beyond this time is small and is neglected in the simulations. The value of Re_λ at this stage is 18. The plasma is then introduced at the centre of the flow field by increasing the temperature and pressure at constant density. Experiments of laser energy deposition in quiescent air (Adelgren, Boguszko & Elliott 2001; Glumac, Elliott & Boguszko 2005) show that energy deposition is symmetric about the laser axis and the plasma generated is initially tear drop shaped. This fact is used to model the initial mean flow. Note that with turbulence in the background, the instantaneous flow field is not axisymmetric. Figure 9(*a*) shows the axial temperature distribution used to model the initial mean temperature profile of the plasma. This temperature distribution is obtained from simulations of Kandala (2005) who models the initial plasma formation in detail. The mean temperature profile perpendicular to the plasma axis is assumed to be a Gaussian. Figure 9(*b*) shows contours of initial mean temperature in a plane passing through the plasma axis. The initial mean pressure field is then obtained from the equation of state through a process of iteration (Ghosh & Mahesh 2008). The ratio of the maximum temperature in the plasma core to the background temperature, T_0 determines the amount of laser energy absorbed by the flow. All simulations reported use a T_0 of 30.

4.1. *Laminar simulation*

A detailed study of laser energy deposition in quiescent air is presented in Ghosh & Mahesh (2008). The more prominent observations are summarized below. Laser

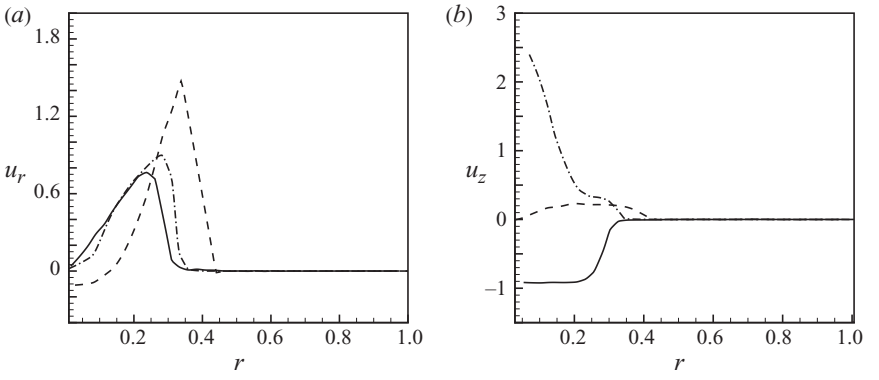

FIGURE 10. Radial profiles at different axial locations at $t = 0.09$: (a) radial velocity u_r, (b) axial velocity u_z, ——— at $z = 2.5$, – – – – at $z = 3.0$, —·— at $z = 3.5$.

energy deposition results in formation of sharp gradients perpendicular to the plasma axis. These gradients accelerate the flow in their direction resulting in the formation of a shock wave. The shock wave then propagates into the back ground, its intensity decreasing with time.

The curvature of the propagating shock wave changes in time. Also the strength of the shock wave changes from one point to another along its surface, and in time. Figure 10 shows radial profiles for different flow variables at $t = 0.09$. Since energy deposition is axisymmetric in nature, an axisymmetric coordinate system is chosen and the flow variables are plotted as a function of r at three different stations $z = 2.5$, 3 and 3.5. Figure 10(a) shows radial profiles for the radial component of velocity u_r. Note the formation of a shock front. Also note that the shock front is strongest and located farthest from the plasma axis for $z = 3.0$ which is close to the centre of the flow domain. This is because the gradients perpendicular to the plasma axis are strongest for this value of z and so maximum flow acceleration occurs here, resulting in the tear drop shape of the shock wave.

The radial variation of the axial velocity component u_z is shown in figure 10(b). Significant expansion is observed along the plasma axis. A centre of expansion is formed close to the centre of the domain and the flow expands around it. The expansion is in opposite directions along the plasma axis. Thus, strong negative velocities are observed close to the axis for $z = 2.5$ and strong positive velocities are observed for $z = 3.5$. The velocity at $z = 3.0$ is close to zero as it is close to the centre of expansion. Since the expansion in the axial direction is localized near the plasma axis, the u_z values soon decrease to zero away from the axis. Radial profiles for pressure and density also show trends similar to u_r.

The shock wave is initially tear drop shaped owing to the initial asymmetry of laser energy deposition (figure 11a). But, as it propagates into the background, there is nothing to sustain this asymmetry and it becomes spherical in shape (figure 11b). Also, its strength gets more evenly distributed across its surface in time. As the shock wave propagates into the background, the flow field behind the shock wave passes through different stages (Ghosh & Mahesh 2008). Figure 12 shows temperature contours at different instants of time. Note that the core of the plasma region breaks along the plasma axis from right to left and eventually rolls up. This trend is observed in laser-induced breakdown experiments (Adelgren *et al.* 2001; Glumac *et al.* 2005). Initially, a centre of expansion is formed in the core (figure 13a). This centre of

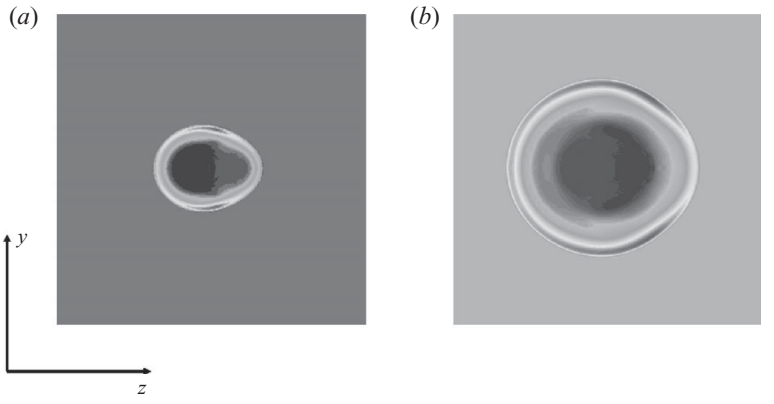

FIGURE 11. Pressure contours at $t = 0.36$ (a) and 0.99 (b) show shock propagation.

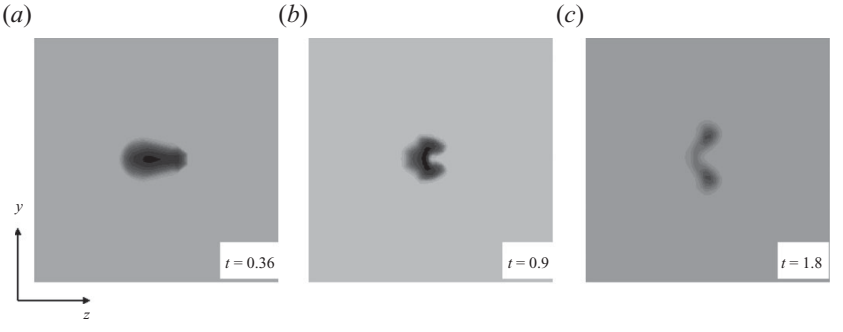

FIGURE 12. Evolution of the temperature field in time.

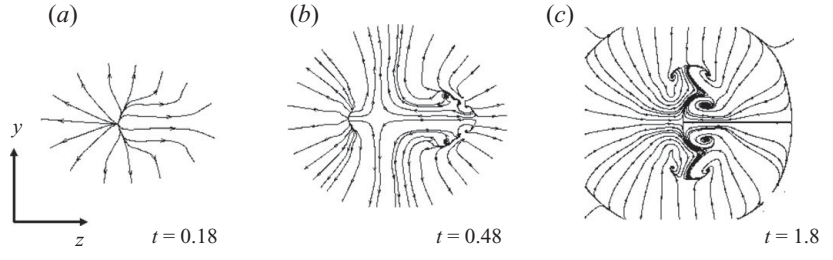

FIGURE 13. Plots of velocity streamlines showing evolution of the flow field in time.

expansion splits into two independent centres of expansion along the plasma axis which compete against each other. The tear drop shape of the shock wave results in asymmetric pressure distribution in the core (figure 11). At later times, higher pressure gradients on the right (figure 11b) result in acceleration of the flow along the axis from right to left (figure 13b). Interaction of this reverse flow with the left expansion point leads to rolling up of the core (figure 13c).

Vorticity is found to be generated by the mean flow at short and long times due to separate mechanisms (figure 26). At short times ($t < 0.30$), propagation of a curved shock wave of varying strength and curvature results in production of baroclinic vorticity. At longer times vorticity is produced due to rolling up of the plasma core. Baroclinic vorticity production is short lived and intense in nature while vorticity produced due to roll up is less intense and more prolonged in time.

4.2. *Effect of turbulence on the mean flow*

Since energy deposition is symmetric about the laser axis, the mean flow is computed in an axisymmetric manner. An axisymmetric mean is defined as

$$\bar{f}(r, z) = \frac{\sum f(\mathscr{X}, \mathscr{Y}, \mathscr{Z})}{N_\theta(r, z)}, \tag{4.5}$$

where the summation is performed over all points in the θ direction for any given value of r and z and N_θ is the number of all such points. Here f denotes any flow variable and r, θ and z are the radial, azimuthal and axial coordinates, respectively. Since the flow field resulting form laser-induced breakdown is highly compressible in nature, Favre averages are used. For any flow variable f, the Favre average is

$$\tilde{f} = \frac{\overline{\rho f}}{\bar{\rho}}, \tag{4.6}$$

where ρ is the fluid density. Recall that in the absence of turbulence, the post energy deposition flow can be categorized into three phases: shock formation, shock propagation and subsequent collapse of the plasma core. When laser energy is deposited in a turbulent background, the turbulent fluctuations affect the evolution of the mean flow during all the three phases. The extent of the effect depends strongly on the M_t of the turbulence. Each stage is studied in detail.

4.2.1. *Shock formation*

During shock formation, part of the deposited laser energy gets converted into kinetic energy resulting in formation of a shock wave. If shock formation occurs in a turbulent background, part of the kinetic energy of the mean flow is transferred to the turbulent background. This results in slowing down of the shock formation process and amplification of the turbulent fluctuations in the vicinity of the shock wave.

The mean kinetic energy equation is studied to understand the mechanism by which energy is transferred from the mean flow to the background turbulence. It is given by

$$\frac{\partial}{\partial t}(\bar{\rho} e_k) = \overline{(\rho \boldsymbol{u}'' \otimes \boldsymbol{u}'')} : \nabla \tilde{\boldsymbol{u}} - \nabla \cdot (\bar{\rho} \tilde{\boldsymbol{u}} e_k) - \nabla \cdot (\tilde{\boldsymbol{u}} \cdot \overline{(\rho \boldsymbol{u}'' \otimes \boldsymbol{u}'')}) - \tilde{\boldsymbol{u}} \cdot \nabla \bar{p} + \tilde{\boldsymbol{u}} \cdot (\nabla \cdot \bar{\boldsymbol{\tau}}), \tag{4.7}$$

where e_k is the mean kinetic energy per unit mass given by $1/2(\tilde{\boldsymbol{u}} \cdot \tilde{\boldsymbol{u}})$ and the emboldened quantities are vectors. In a laminar background, the first and the third terms on the right-hand side of the above equation drop out. The fourth (pressure gradient) term indicates that presence of negative pressure gradients will result in amplification of kinetic energy. This occurs during the shock formation phase and amplification of kinetic energy results in the formation of a shock front.

When shock formation occurs in presence of turbulence in the background, the production term which is the first term on the right-hand side of (4.7) becomes important. Note that this term occurs with opposite signs on the right-hand sides of both mean and turbulent (defined in (4.10)) kinetic energy equations. Section 4.5 contains a discussion on budgets for different terms on the right-hand side of the turbulent kinetic energy equation. Figure 14(*a*) shows that $-\overline{(\rho \boldsymbol{u}'' \otimes \boldsymbol{u}'')} : \nabla \tilde{\boldsymbol{u}}$ is positive near the shock wave. This results in decrease in mean kinetic energy and increase in turbulent kinetic energy near the shock wave (from (4.7) and (4.10)). Thus the production term acts as means for transfer of energy from the mean flow to

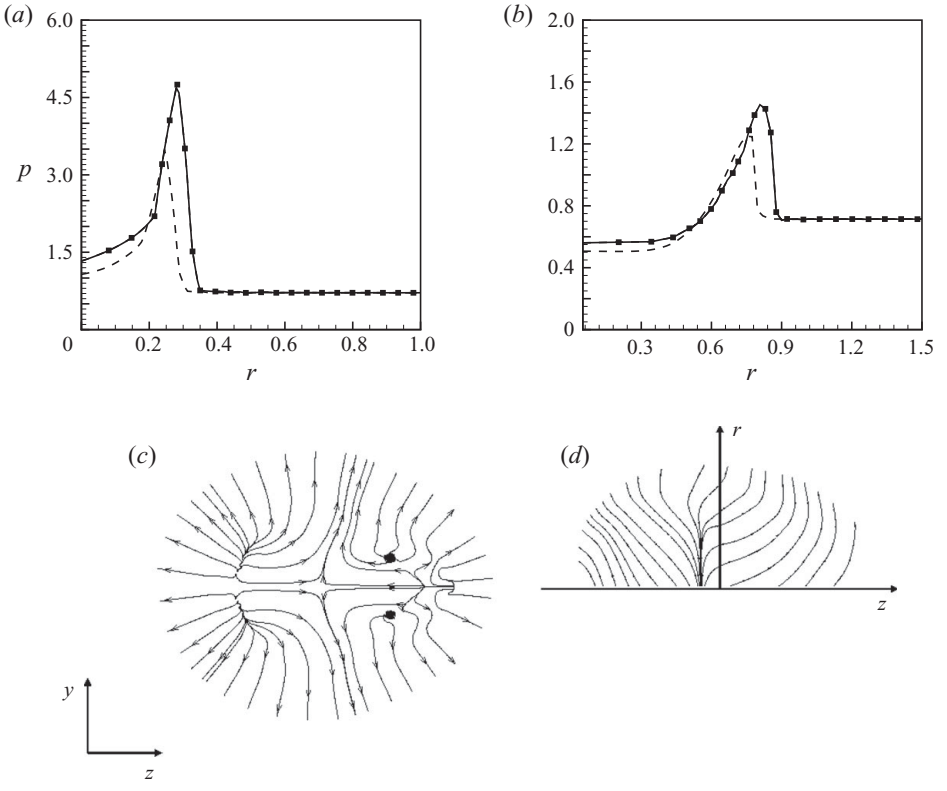

FIGURE 14. Effect of turbulence on the mean flow: (*a*) radial profiles for pressure at the end of shock formation; (*b*) radial profiles for pressure during shock propagation ($t = 0.36$), ■: Laminar, ——— : $M_t = 0.001$, - - - - : $M_t = 0.3$; (*c*) velocity streamlines for laminar solution at $t = 0.36$; (*d*) mean velocity streamlines for the turbulent simulations with $M_t = 0.3$ at $t = 0.36$ showing no core roll up.

the turbulent background. The net effect of pressure gradient and production terms results in shock formation at a slower rate.

Note that the effect of the production term depends on the intensity of the background turbulence and is much smaller for the $M_t = 0.001$ case compared to that for the $M_t = 0.3$ case. This is evident from figure 14(*a*). Radial profiles of pressure are shown at the end of shock formation for the laminar flow, for the $M_t = 0.001$ case and for the $M_t = 0.3$ case. Note that the profile for the $M_t = 0.001$ case lies very close to that for the laminar flow. However, the pressure profile for the $M_t = 0.3$ case shows that the peak value of pressure obtained at the end of shock formation is significantly less compared to the laminar flow. Also, the shock wave is observed to be formed at a radial location closer to the plasma axis. The effect of the turbulent fluctuations on shock formation is evident in other flow variables as well. Table 1 provides maximum values of different flow variables at the end of shock formation.

4.2.2. *Shock propagation*

After a shock wave is formed, it propagates into the background with decreasing strength due to the radial nature of its propagation. In the presence of turbulence,

Case	Shock formation time	Maximum velocity at shock front	Maximum pressure at shock front	Maximum density at shock front
Laminar	0.05	2.4	4.75	2.8
Turbulent ($M_t = 0.001$)	0.05	2.4	4.74	2.8
Turbulent ($M_t = 0.3$)	0.06	0.6	3.5	1.84

TABLE 1. Effect of turbulence on shock formation.

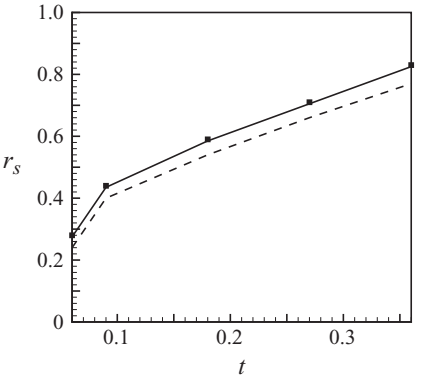

FIGURE 15. Shock radius in time: ■: Laminar, ——— : $M_t = 0.001$, – – – – : $M_t = 0.3$.

the production term of (4.7) removes energy from the mean flow resulting in further slowing down of the shock wave. Again, the extent to which shock propagation is slowed down by the turbulence is much larger for the $M_t = 0.3$ case.

Figure 14(b) shows radial profiles for pressure at $t = 0.36$ for the laminar flow, for $M_t = 0.001$ and for $M_t = 0.3$. The pressure profile for $M_t = 0.001$ almost coincides with the profile for laminar flow showing that the mean flow is almost unaffected by the turbulent fluctuations in this case. However, the pressure profile for $M_t = 0.3$ shows that the shock wave has further slowed down as a result of interaction with the turbulent background.

Figure 15 compares the variation of shock radius in time for the $M_t = 0.001$ and 0.3 cases to the laminar case during the shock propagation stage. The shock radius variation for the low M_t case is almost same as the laminar solution. The high M_t case on the other hand shows that the shock wave is slowed down by the turbulent background both during shock formation and propagation. Also, the difference between the laminar and turbulent shock radii is small at short times and increases with time.

Table 2 provides values of different flow variables when the shock wave reaches a radial distance $r = 1$ from the plasma axis. This value of r is chosen so that the shock wave and its effect on the turbulence stays sufficiently far away from the domain boundaries and are not affected by the periodic boundary conditions. Shock propagation time is then defined as the time required by the shock wave to reach $r = 1$ from its location at the end of shock formation. For the $M_t = 0.3$ case, the shock propagation time is larger and the values for maximum velocity, pressure and density at $r = 1$ are smaller compared to the other cases.

Case	Shock propagation time	Maximum velocity at $r = 1$	Maximum pressure at $r = 1$	Maximum density at $r = 1$
Laminar	0.45	0.54	1.3	1.6
Turbulent ($M_t = 0.001$)	0.45	0.54	1.3	1.6
Turbulent ($M_t = 0.3$)	0.48	0.42	1.1	1.35

TABLE 2. Effect of turbulence on shock propagation.

Case	T_0	$(P_{max})_{SF}$
Laminar	30	4.75
Turbulent ($M_t = 0.001$)	30	4.74
Turbulent ($M_t = 0.3$)	30	3.5
Laminar	25.5	3.46

TABLE 3. Table of parameters for laminar simulation at lower energy level.

4.2.3. *Roll up*

During shock propagation in a quiescent background, the plasma core behind the shock wave passes through different stages eventually resulting in rolling up of the core. These stages have been described in § 4.1. In the presence of turbulence, depending on the M_t of the turbulent flow, the turbulent fluctuations can affect the evolution of the core significantly. In the case of $M_t = 0.001$ the evolution of the core is not much affected and hence it is very similar to the that observed for the laminar flow. This is evident from instantaneous velocity streamlines shown in figure 18. Note that the velocity streamlines near the core evolve very similar to the laminar velocity streamlines.

However, for the $M_t = 0.3$ case, the evolution of the plasma core is very different. Figure 14(d) shows velocity streamlines for the mean flow at $t = 0.36$. Only the top half of the flow field above the plasma axis is shown. A comparison with the laminar velocity streamlines (figure 14c) obtained at that instant shows absence of distinct expansion points along the plasma axis. As described in § 4.1, these expansion points lead to acceleration of the flow along the plasma axis from right to left eventually resulting in the plasma core rolling up. Thus, absence of these expansion points result in the mean flow not rolling up in time for the $M_t = 0.3$ case.

Since substantial amount of energy is removed from the mean flow for the $M_t = 0.3$ case, a laminar simulation at a lower energy level is performed to ensure that the lack of late time core roll up is not unrelated to the turbulence evolution. The T_0 for this simulation is determined by matching maximum pressure at the end of shock formation (figure 14a) to that for the $M_t = 0.3$ case and is obtained as 25.5 (table 3). Figure 16(a) shows temperature contours obtained from this simulation at $t = 2.1$. The core is observed to roll up suggesting that the lack of late time roll up for the $M_t = 0.3$ turbulent simulation is not due to lower mean energy level.

The change in shape of the mean shock wave due to interaction with the turbulent background could also suppress core roll up for the $M_t = 0.3$ case. Roll up is caused by a reverse flow (right to left) along the laser axis (§ 4.1). This is a result of asymmetric pressure distribution in the core behind the shock wave and depends on

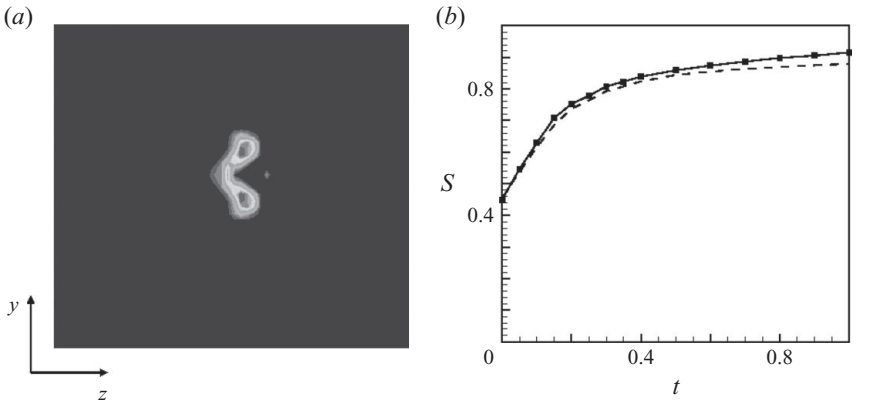

FIGURE 16. (*a*) Temperature contours for the low energy laminar simulation. (*b*) Evolution of shock symmetry S in time: ——— : laminar, ■ : turbulent ($M_t = 0.001$), – – – – : turbulent ($M_t = 0.3$).

the asymmetry of the tear drop shock shape. Here symmetry is considered about the vertical central plane. Defining an asymmetry variable S as the ratio of the maximum extent of the shock wave perpendicular to the laser axis to that along the laser axis, time evolution of S is shown in figure 16(*b*). It is found that while for the $M_t = 0.001$ case the shock shape is not much affected, for the $M_t = 0.3$ case the shock shape becomes more asymmetric in time upon interaction with the turbulence. This can be explained based on the fact that stronger velocity gradients perpendicular to the laser axis result in removal of more energy from the mean flow through the production term thus slowing down the shock wave more in this direction. A more asymmetric shock wave generates a more asymmetric pressure distribution in the core and should not be the reason for suppression of core roll up for the $M_t = 0.3$ case.

4.3. *Effect on the turbulence*

4.3.1. *Computation of turbulent statistics*

Since laser energy deposition is axisymmetric in nature, turbulent statistics are computed axisymmetrically. Any flow variable f is decomposed about its average as

$$f = \widetilde{f} + f'', \tag{4.8}$$

where $\widetilde{f}$ is the Favre average (§4.2) of f and f'' represents the fluctuations in f about $\widetilde{f}$. At any given radial location r and axial location z, the turbulent statistics are computed by summing up values of flow variables at all the points lying in the azimuthal direction. If the values of r and z are such that they lie on the shock front then due to the distortion of the shock wave by the turbulence, some of the points in the azimuthal direction would lie upstream of the shock wave while others would lie downstream of it. The statistics thus computed at this r and z location will be of very high magnitude and will no longer represent true turbulent fluctuation. Figure 17 demonstrates this effect. Azimuthal distribution of the instantaneous pressure field is shown at the shock front for $t = 0.09$. Note that even though the real turbulent fluctuations are of small magnitude, the fact that not all points lie on the same side of the shock wave results in erroneously high values for the turbulent statistics. Similar behaviour has been observed in direct numerical simulations of shock/turbulence interaction (Lee *et al.* 1993; Mahesh *et al.* 1997).

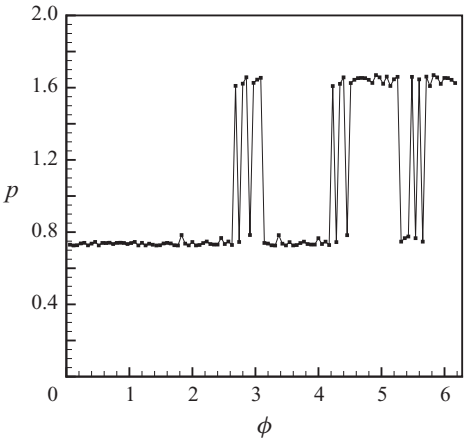

FIGURE 17. Instantaneous spread of the pressure field in the azimuthal direction at the shock front for the $M_t = 0.001$ case. Here $z = 3.14$, $r = 0.4$ and $t = 0.09$.

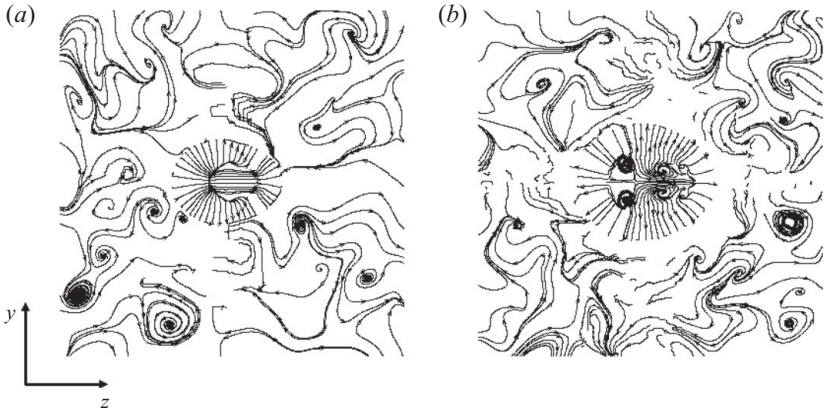

FIGURE 18. Velocity streamlines showing instantaneous flow field at (*a*) $t = 0.18$ and (*b*) $t = 0.81$ for $M_t = 0.001$.

4.3.2. *Results for* $M_t = 0.001$

For a fluctuation Mach number of 0.001, the r.m.s. velocity as defined in §4 is obtained as 20 cm s^{-1}. Thus, while the plasma evolves on a rate comparable to the acoustic time scale, the turbulence on the other hand evolves at a much slower rate. The eddy turn-over time for the turbulence is computed as $\lambda/u_{rms} \simeq 693$ while the time required by the blast wave to reach the domain boundaries is $O(1)$.

This difference in flow evolution time scales is evident from instantaneous flow fields shown in figures 18(*a*) and 18(*b*). Velocity streamlines are shown at $t = 0.18$ and 0.81. Expansion of the post breakdown plasma core observed in figure 18(*a*) generates velocities of $O(1)$ in the core, while the turbulent fluctuations of the core prior to energy deposition were of $O(10^{-3})$. The shock wave formed at the edge of the expanding core strongly compresses the turbulence in its vicinity. As the shock wave propagates into the background, the core behind it evolves as observed in the laminar simulations in §4.1 to eventually roll up (figure 18*b*). Note that as the mean flow evolves through different stages, the turbulence ahead of the blast wave is 'frozen' for

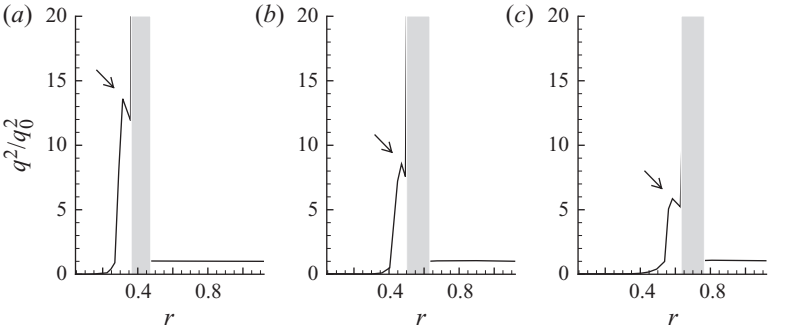

FIGURE 19. Radial profiles of turbulent kinetic energy at $t = 0.09$ (*a*), 0.18 (*b*) and 0.27 (*c*) for $M_t = 0.001$.

all practical purposes and does not have a significant effect on the evolution of the mean flow.

The effect of the mean flow on the turbulence is spatially inhomogeneous and statistically non-stationary in nature. Figure 19 shows radial profiles of the turbulent kinetic energy computed at $z = 3.14$ for three different time instants. The turbulent kinetic energy is normalized with respect to its background initial value. Turbulent kinetic energy is obtained as

$$q^2 = \widetilde{u_r''^2} + \widetilde{u_\theta''^2} + \widetilde{u_z''^2}, \tag{4.9}$$

where u_r'', u_θ'' and u_z'' are velocity fluctuations along the r, θ and z coordinate directions.

As the shock wave propagates into the background its intensity decreases in time. At any given time, compression near the shock wave results in amplification of the turbulence levels. Recall that similar amplification in vorticity due to compression was observed for the model single vortex problem described in § 3. In the case of the single vortex problem, budgets for the vorticity equation showed that the bulk dilatation term was responsible for the amplification of vorticity levels. For the turbulent problem, production and pressure dilatation are the primary causes for amplification of turbulent kinetic energy behind the shock wave. This is described in detail in § 4.5 where budgets are computed for different terms on the right-hand side of the turbulent kinetic energy equation.

Amplification of turbulence levels behind the shock front is consistent with linear analysis of a shock wave interacting with isotropic turbulence (Lee *et al.* 1993, 1997; Mahesh *et al.* 1994, 1995, 1997). It is quite instructive to consider the upstream turbulence as a combination of vorticity, acoustic and entropy modes and to describe shock/turbulence interaction in terms of the independent interaction of each of these modes with the shock wave. Linear analysis based on such modal decomposition shows that bulk compression increases turbulence levels while baroclinic effects can either increase or decrease turbulence amplification depending on the sign of the velocity–temperature correlation (Mahesh *et al.* 1997). At any instant, the q^2 profile increases sharply to a maximum and then decreases slightly behind the shock front. Thus the maximum amplification is not obtained at the shock front but behind it. This is shown using arrows in figures 19 and 20. Figure 19 shows that as the shock strength decreases, the amplification of turbulence levels also decrease in time. Note

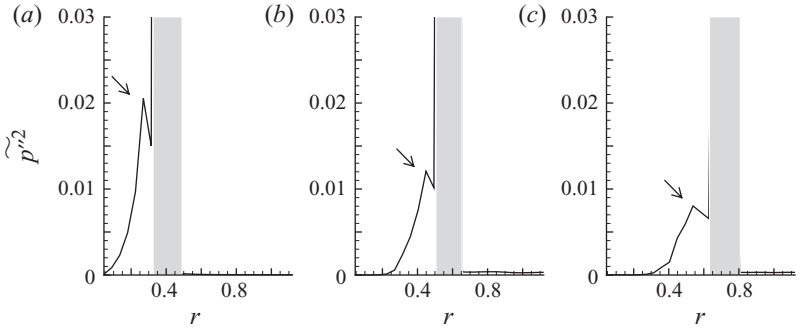

FIGURE 20. Radial profiles of pressure fluctuations at $t = 0.09$ (a), 0.18 (b) and 0.27 (c) for $M_t = 0.001$.

that amplification as high as approximately 15 times the initial background value is observed at $t = 0.09$. The strong amplification is due to the strong shock wave.

Figure 20 shows radial profiles for $\widetilde{p''^2}$. The pressure fluctuations are also observed to amplify near the shock wave and the extent of amplification is found to decrease in time. At any given time, the $\widetilde{p''^2}$ profile in the radial direction is very similar to the q^2 profile. Since the core of the plasma experiences strong expansion, the turbulence intensities near the core are suppressed in time (figures 19 and 20). Note that the effect of expansion near the core is much more prolonged than the effect of compression near the shock wave and hence the former relaxes on a much larger time scale as compared to the latter. Note that in both figures 19 and 20, the turbulent statistics at the shock front are shaded out. This is because the statistics at the shock front do not represent real turbulence as described in § 4.3.1.

At any given time, the strength of the shock wave varies across its surface. Thus the compression of the turbulence and the amplification in its intensities also vary across the surface of the shock wave. Figure 21(a) shows the angular distribution of the maximum value of $q^2/{q_0}^2$ for $t = 0.09$, 0.18 and 0.27. Here, the angle ϕ is defined with respect to the plasma centre and measured away from the plasma axis from right to left (figure 21c). The angular profiles are computed by obtaining the maximum value of a flow variable behind the shock wave along different ϕ directions. Maximum q^2 amplification is obtained for $\phi > 90^\circ$ at $t = 0.09$ and in time the location of the peak is observed to move from right to left in figure 21(a). This is because the shock strength is maximum for $\phi > 90^\circ$ at early times as a result of balance between the expansion along the plasma axis and expansion perpendicular to it (Ghosh & Mahesh 2008). In time as the shock wave becomes spherical, the peak shock strength shifts from right to left resulting in a similar shift in the profiles of q^2.

Angular profiles for the maximum value of $\widetilde{p''^2}$ also show similar trends (figure 21b). The maximum amplification in the pressure fluctuations is observed for $\phi > 90^\circ$ and in time the peak shifts towards $\phi = 90^\circ$. Note that over time the angular distribution of both $q^2/{q_0}^2$ and $\widetilde{p''^2}$ do not change very much.

4.3.3. *Results for* $M_t = 0.3$

When the fluctuation Mach number is 0.3, the turbulence evolves on a time scale comparable to that of the plasma. The eddy turn over time for the turbulence is approximately twice the time required by the shock wave to reach the domain

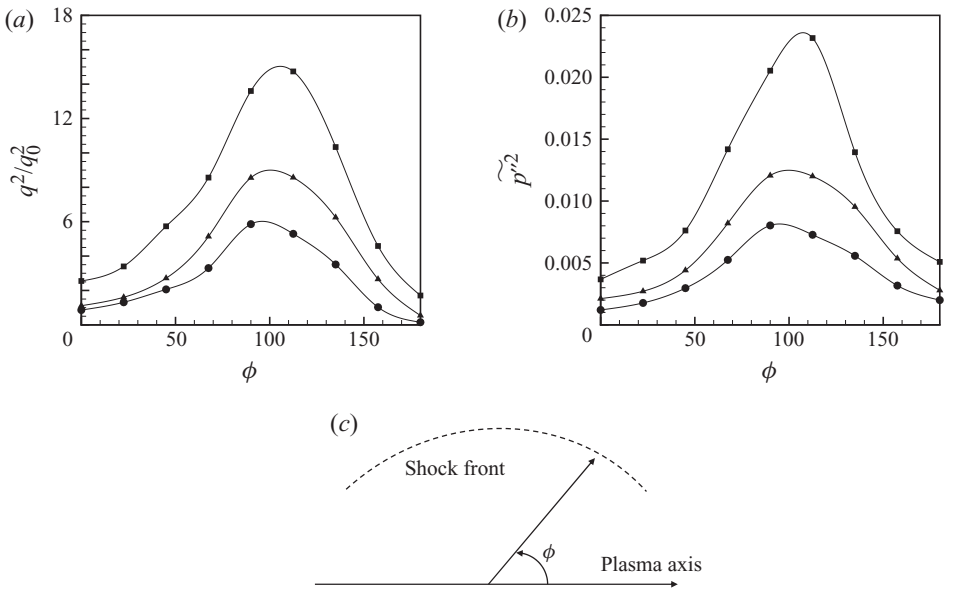

FIGURE 21. Angular profiles of (*a*) $q^2/{q_0}^2$ and (*b*) $\widetilde{p''^2}$ in time for $M_t = 0.001$, ■ at $t = 0.09$, ▲ at $t = 0.18$, ● at $t = 0.27$; (*c*) Schematic showing the definition of ϕ.

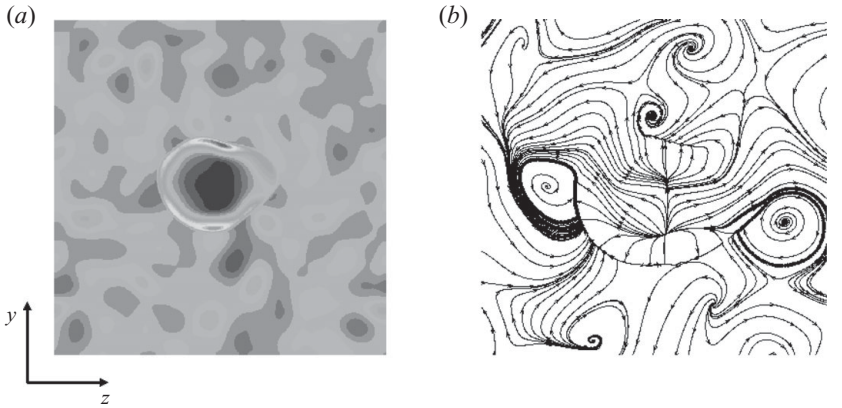

FIGURE 22. Instantaneous flow field: (*a*) pressure contours and (*b*) velocity streamlines at $t = 0.36$ for $M_t = 0.3$.

boundaries. Also, the turbulent fluctuations are comparable in magnitude to the mean flow velocities as opposed to $M_t = 0.001$ discussed in § 4.3.2.

Figure 22(*a*) shows instantaneous contours of pressure at $t = 0.36$. Note that as the shock wave propagates, it interacts strongly with the background turbulence. Both the shock wave and the core are heavily distorted as a result of this interaction. As the shock wave propagates into the background, it becomes spherical in shape. Its intensity decreases at a much faster rate compared to the decay rate of the turbulence. Thus when the shock wave becomes weak enough, interaction with the relatively strong turbulent fluctuations results in disintegration of the shock wave.

Figure 22(*b*) shows velocity streamlines at the same instant of time. Velocities generated as a result of core expansion are of the same order of magnitude as the turbulent fluctuations. Thus even though the plasma core is visible in figure 22(*b*), it

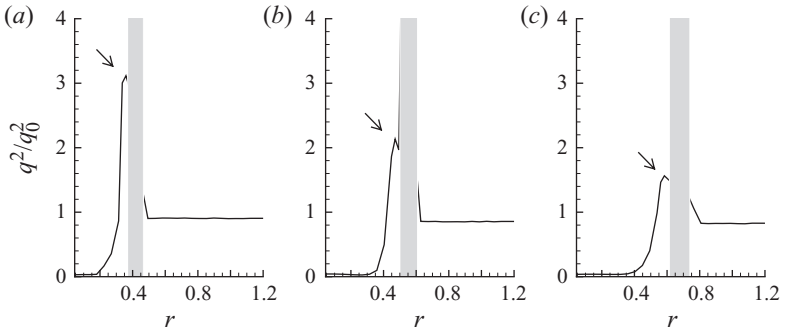

FIGURE 23. Radial profiles of turbulent kinetic energy at $t = 0.09$ (a), 0.18 (b) and 0.27 (c) for $M_t = 0.3$.

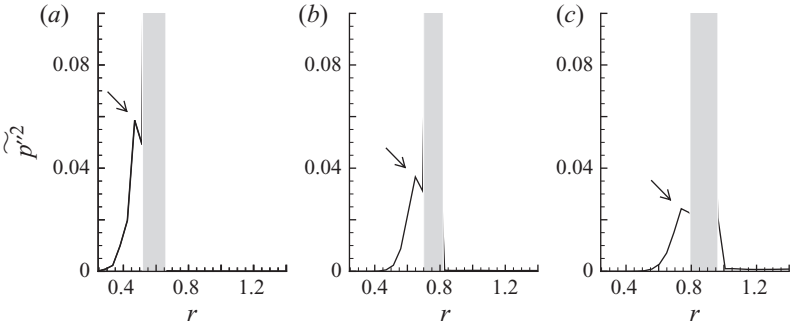

FIGURE 24. Radial profiles of pressure fluctuations at $t = 0.09$ (a), 0.18 (b) and 0.27 (c) for $M_t = 0.3$.

is not as distinct as observed in figure 18. In fact, the core interacts so strongly with the turbulence that it does not undergo the characteristic flow evolution sequence (§ 4.1) and hence does not roll up in time as discussed in § 4.2.3.

Figure 23 shows radial profiles for turbulent kinetic energy $\widetilde{q^2/q_0{}^2}$ while figure 24 shows radial profiles for pressure fluctuations $\widetilde{p''^2}$ at three different instants of time. The profiles are obtained at $z = 3.14$. These profiles are similar to those obtained in the case of $M_t = 0.001$. At any given time the profiles start close to zero near the core indicating significant expansion. With increase in r the profiles increase sharply to a maximum and then decrease slightly behind the shock front. This is due to the effect of compression caused by the pressure gradients at and behind the shock wave and is similar to the compression-induced amplification of vorticity levels observed for the model single vortex problem described in § 3.

The maximum value obtained for $\widetilde{q^2/q_0{}^2}$ is approximately 3.2 which is much smaller compared to that obtained in § 4.3.2. This is because the shock wave is much weaker after interaction with the high M_t turbulence (§ 4.2). Also, the turbulence time scale is much more comparable to the time scale of the shock wave. So at $t = 0.09$ the turbulence has evolved to a much later stage compared to the $M_t = 0.001$ case where the effect of the shock wave was more sudden in nature and the turbulence did not get sufficient time to react. However, the absolute values for $\widetilde{q^2}$ and $\widetilde{p''^2}$ are higher than those obtained for the $M_t = 0.001$ case. Note that the effect of expansion on the core relaxes at a much slower rate when compared to the effect of compression in the vicinity of the shock wave.

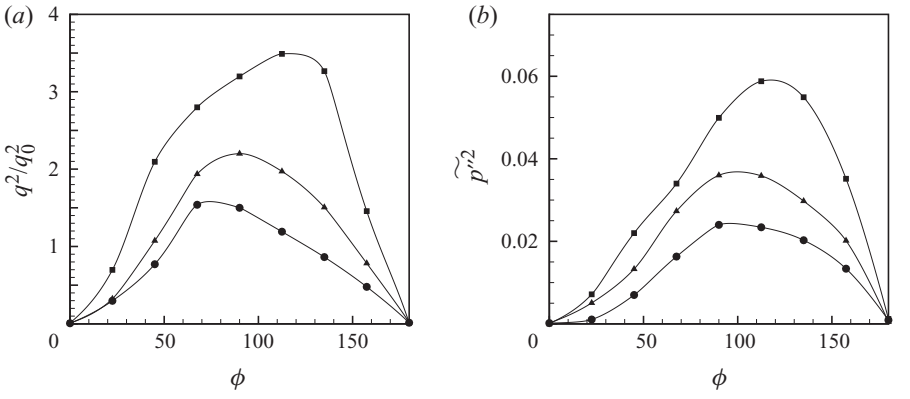

FIGURE 25. Angular profiles of (*a*) $q^2/{q_0}^2$ and (*b*) $\widetilde{p''^2}$ in time for $M_t = 0.3$, ■ at $t = 0.09$, ▲ at $t = 0.18$, ● at $t = 0.27$.

Figures 25(*a*) and 25(*b*) show angular distribution of the maximum values of $q^2/{q_0}^2$ and $\widetilde{p''^2}$ respectively at $t = 0.09$, 0.18 and 0.27, respectively. The angle ϕ is defined in figure 21(*c*). The angular profiles are also similar to those obtained for the $M_t = 0.001$ case. The profiles are observed to peak for $\phi > 90^\circ$ at $t = 0.09$ and the peak is observed to shift towards $\phi = 90^\circ$ in time.

4.4. *Vorticity field*

For the laminar problem, vorticity is generated in the flow by different processes at different times. Propagation of a curved shock wave of varying strength and curvature results in production of baroclinic vorticity in the flow. Since both strength and curvature of the shock wave varies in time, the magnitude of baroclinic vorticity generated also varies in time and is significant for $t < 0.3$. At longer times, the collapse of the plasma core described in § 4.1 generates vorticity. Figure 26(*a*) shows the time evolution of maximum vorticity magnitude in the case of a laminar simulation. The first peak corresponds to baroclinic vorticity production while the second peak corresponds to production of vorticity due to the rolling up of the plasma core.

When laser energy is deposited in a turbulent background both $M_t = 0.001$ and 0.3 cases produce mean vorticity at short times due to baroclinic effects. However, secondary vorticity production due to core roll up is suppressed for the $M_t = 0.3$ case. This is because as described in § 4.2.3, the mean flow in this case is significantly affected by the turbulent fluctuations and does not roll up in time. Figure 26(*b*) shows velocity streamlines plotted over contours of vorticity magnitude at $t = 1.2$ for the $M_t = 0.001$ case. Core streamlines show roll up while vorticity contours show vorticity amplification in the core.

The Q criterion for vortex identification is also used to show secondary vorticity production in the core at long times for the $M_t = 0.001$ case and absence of the same for the $M_t = 0.3$ case. Isocontours of $Q > 0$ are plotted for the two cases at $t = 1.2$. Q isocontours for the $M_t = 0.001$ case (figure 26*c*) show amplification of vorticity levels near the core due to roll up. No such amplification in vorticity levels is observed from the Q isocontours for the $M_t = 0.3$ case (figure 26*d*) and only the background turbulent vorticity is observed.

Vorticity generated by the mean flow results in the amplification of turbulence levels. Figure 26(*e*) shows the maximum value for vorticity magnitude fluctuations in time. The vorticity fluctuations are sharply amplified at short times as a result of

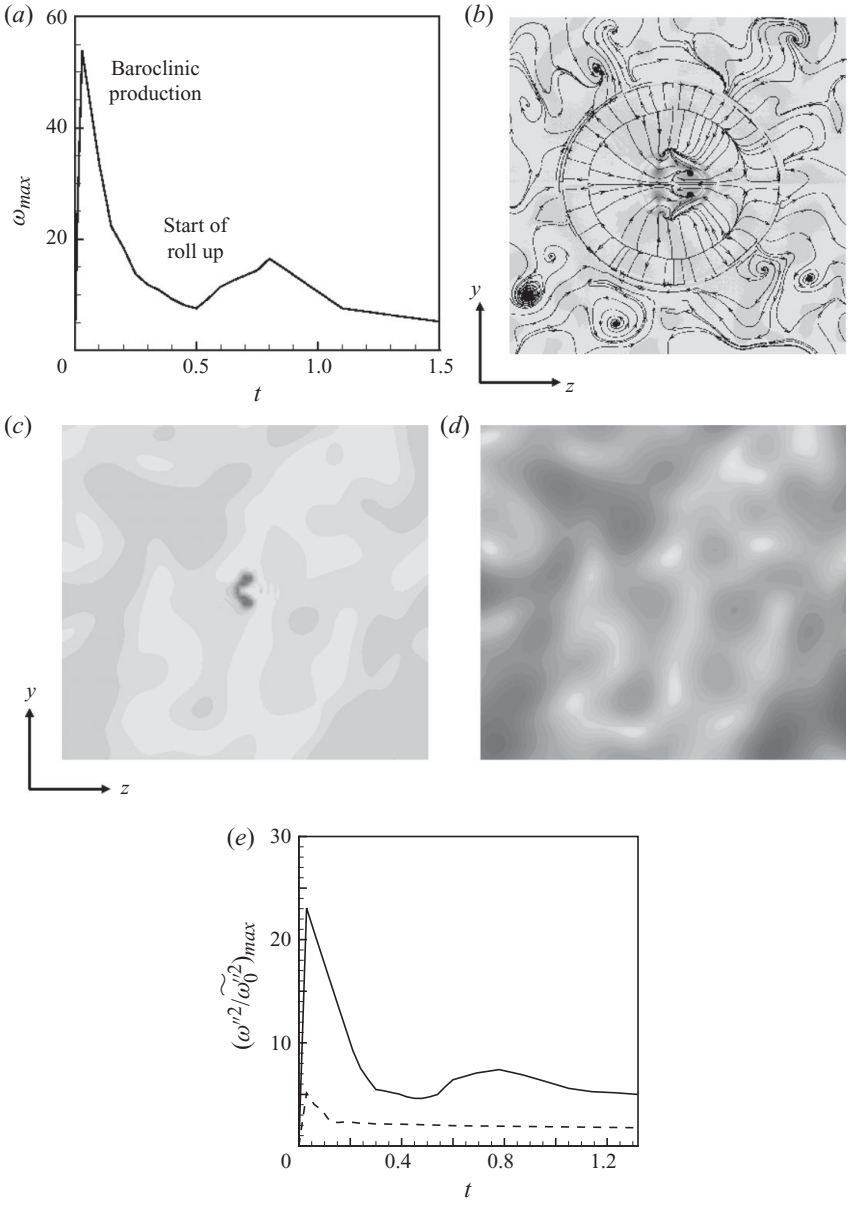

FIGURE 26. Vorticity generated in the flow: (*a*) evolution of maximum vorticity magnitude in time for laminar simulation, (*b*) velocity streamlines plotted over contours of vorticity magnitude at $t = 1.2$ for $M_t = 0.001$ showing vorticity generation due to roll up at long times, (*c*) isocontours of Q for $M_t = 0.001$ showing secondary vorticity generation in core at $t = 1.2$, (*d*) isocontours of Q for $M_t = 0.3$ showing absence of secondary vorticity generation in core, (*e*) evolution of maximum vorticity magnitude fluctuations in time for ——— : $M_t = 0.001$ and - - - - : $M_t = 0.3$.

baroclinic production. This amplification is observed near the leading and trailing edges of the plasma region for both $M_t = 0.001$ and 0.3. At longer times, $M_t = 0.001$ shows a second peak representing roll up of the plasma core. The secondary vorticity amplification is weaker in magnitude compared to the baroclinic amplification and

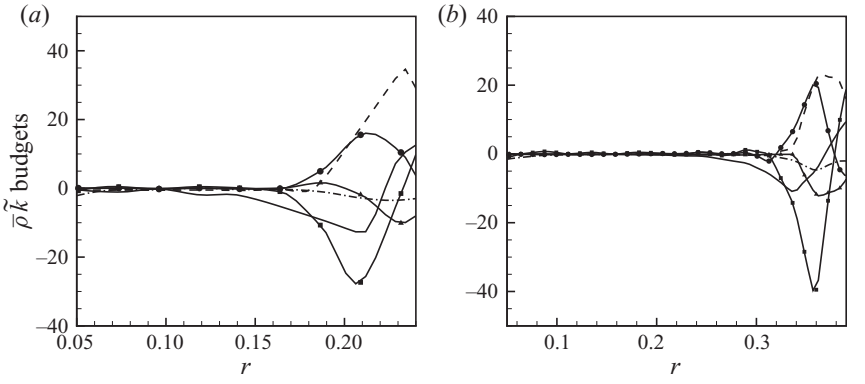

FIGURE 27. Radial profiles showing the turbulent kinetic energy budget at $z = 3.14$ during (*a*) shock formation ($t = 0.03$) and (*b*) shock propagation ($t = 0.09$): ——— : convection, – – – – : production, —·— : dissipation, ■ : diffusion, ▲ : pressure work, ● : pressure dilatation.

lasts longer in time. The plot for the $M_t = 0.3$ case does not show secondary amplification at longer times due to the absence of secondary vorticity generation in the mean.

4.5. *Turbulent kinetic energy budgets*

Budgets are computed for different terms on the right-hand side of the turbulent kinetic energy equation. The $M_t = 0.3$ case is considered. Transport equation for turbulent kinetic energy can be written as

$$\frac{\partial}{\partial t}(\bar{\rho}\widetilde{k}) = \underbrace{-\nabla\cdot(\bar{\rho}\bar{\boldsymbol{u}}\widetilde{k})}_{\text{Convection}} \underbrace{-\overline{(\rho\boldsymbol{u}''\otimes\boldsymbol{u}'')}:\nabla\widetilde{\boldsymbol{u}}}_{\text{Production}} \underbrace{-\overline{\boldsymbol{\tau}:\nabla\boldsymbol{u}''}}_{\text{Dissipation}}$$
$$\underbrace{+\nabla\cdot\left[\overline{\boldsymbol{u}''\cdot\boldsymbol{\tau}} - \overline{\rho\boldsymbol{u}''\left(\frac{1}{2}\boldsymbol{u}''\cdot\boldsymbol{u}''\right)} - \overline{p'\boldsymbol{u}''}\right]}_{\text{Diffusion}} \underbrace{-\overline{\boldsymbol{u}''}\cdot\nabla(\bar{p})}_{\text{Pressure work}} + \underbrace{\overline{p'\nabla\cdot\boldsymbol{u}''}}_{\text{Pressure dilatation}} . \tag{4.10}$$

The rate of change of turbulent kinetic energy with time is balanced by the convection, production, dissipation, diffusion, pressure work and pressure dilatation terms. Here k is given by $1/2(\boldsymbol{u}''\cdot\boldsymbol{u}'')$ and the emboldened quantities are vectors.

Figure 27 shows radial profiles of different terms on the right-hand side of the above equation at two different instants of time. Profiles are plotted up to a radial location just behind the shock front. This is because the profiles are contaminated at the shock front due to intermittency effects caused by distortion of the shock wave (§ 4.3.1).

Figure 27(*a*) shows the turbulent kinetic energy budget at an instant during shock formation. A comparison with the model single vortex problem studied in § 3 shows that the roles of the production and pressure dilatation terms are similar to that of the bulk dilatation term for the vortex problem. The role of the diffusion term is similar to that of the viscous term for the vortex problem. The production term is positive near the shock front and uses energy from the mean flow to increase the turbulent kinetic energy behind the shock wave. A positive pressure dilatation also results in reversible energy transfer from the mean internal energy to the turbulent

kinetic energy. The diffusion term is dominated by contribution from the pressure part and helps redistribute the turbulent kinetic energy in the radial direction. Note that the production term peaks right behind the shock front while the diffusion term peaks further behind it. Also, sum of the production and pressure dilatation terms dominates the diffusion term and so turbulent kinetic energy amplification behind the shock front increases with time. The convection term plays a role similar to that of the convection term for the vortex problem rearranging the distribution of turbulent kinetic energy in the radial direction.

Figure 27(*b*) shows budgets for turbulent kinetic energy during propagation of the shock wave. Note that immediately behind the shock wave, the production term is the dominant term and its magnitude is much smaller compared to that observed during shock formation. Hence turbulent kinetic energy amplifies behind the shock front but at a decreasing rate (figure 23*a*). At radial locations further behind the shock front, the diffusion term is observed to dominate the collective effects of the production and pressure dilatation terms. Thus, at this radial location the turbulent kinetic energy is decreasing. During both formation and propagation of the shock wave, the production term transfers energy from the mean flow to the turbulence resulting in the decrease in mean kinetic energy and increase in turbulent kinetic energy behind the shock front (§ 4.2).

It is worth mentioning here that the budgets obtained in this case are very different from those obtained for a steady normal shock wave interacting with isotropic turbulence (Lee *et al.* 1993). In the latter case, the net turbulent kinetic energy does not change with time and so the convection term balances all the other terms on the right-hand side of the turbulent kinetic energy equation. Viscous dissipation is found to be the dominant term and the only other term of comparable magnitude is the pressure work term. But in the case of shock wave generated by laser-induced breakdown, these terms are small compared to the production, pressure dilatation and diffusion terms.

5. Summary

The effect of laser energy deposition on isotropic turbulence is studied in this paper. A model two-dimensional problem involving the interaction of an energy deposition region with an isolated vortex is studied as a first step. Shock wave resulting from energy deposition is found to compress the vortex increasing its vorticity. Expansion behind the shock wave is found to suppress its vorticity. Budgets are computed for the laminar vorticity equation to identify the major factors responsible for the amplification and suppression of vorticity levels. The results are used to explain some aspects of laser energy deposition in isotropic turbulence.

Laminar simulation of laser energy deposition in quiescent air is discussed briefly. Laser energy deposition in isotropic turbulence is studied for $Re_\lambda = 30$ and $M_t = 0.001$ and 0.3. For both cases, a shock wave is observed to propagate into the background compressing the turbulence. Significant expansion is observed in the core.

The effect of turbulence on the mean flow is studied in detail. Evolution of the mean flow resulting from laser-induced breakdown is broken into shock formation, shock propagation and roll up of the core. Energy is found to be transferred from the mean flow to the turbulent background through the production term which appears with opposite sign on both mean and turbulent kinetic energy equations. This effect is shown to be much stronger for the $M_t = 0.3$ case due to higher turbulent intensities in the background. Thus shock formation and propagation are found to slow down

for this case and the core is found to not roll up in time. Suppression of mean core roll up for the $M_t = 0.3$ case is also explored based on energy level of the mean flow and mean shock shape.

Turbulence intensities are observed to get amplified due to compression near the shock wave. This behaviour is explained based on the effect of energy deposition on a single vortex. Radial profiles for turbulent kinetic energy and pressure fluctuations are found to peak behind the shock front. The amplification of turbulence near the shock wave is found to decrease in time due to decreasing strength of the shock wave. Also, compression resulting from the shock wave is found to be spatially inhomogeneous. Effect of mean vorticity production on the turbulence is also studied and absence of core roll up for the $M_t = 0.3$ case is shown to result in no secondary amplification of turbulence levels in the core at long times.

Budgets are computed for different terms on the right-hand side of the turbulent kinetic energy equation for the $M_t = 0.3$ case. Radial profiles for the different terms are presented during shock formation and propagation. During shock formation, the sum of the production and pressure dilatation terms dominates the diffusion term and so turbulent kinetic energy amplification behind the shock front is found to increase with time. During shock propagation, the production term is found to dominate immediately behind the shock wave resulting in amplification of turbulence kinetic energy there. Further behind the shock wave, the diffusion term is observed to dominate the collective effects of the production and pressure dilatation terms resulting in a decrease of turbulent kinetic energy there. During both formation and propagation of the shock wave, energy is transferred from the mean flow to the turbulence resulting in slowing down of the mean flow.

This work is supported by the United States Air Force Office of Scientific Research under grant FA9550-04-1-0341 and FA-9550-04-1-0064. Computing resources were provided by the Minnesota Supercomputing Institute, the San Diego Supercomputing centre and the National centre for Supercomputing Applications.

REFERENCES

Adelgren, R., Boguszko, M., Elliott, G. & Knight, D. 2001 Experimental summary report – shock propagation measurements for ND: YAG laser induced breakdown in quiescent air. RU-TR-MAE-214. Department of Mechanical and Aerospace Engineering, Rutgers University.

Adelgren, R. G., Yan, H., Elliott, G. S., Knight, D., Beutner, T. J., Zheltovodov, A., Ivanov, M. & Khotyanovsky, D. 2003 Localized flow control by laser energy deposition applied to Edney IV shock impingement and intersecting shocks. *Paper* 2003–31. AIAA.

Agui, J. H. 1998 Shock wave interactions with turbulence and vortices. PhD thesis, City University, New York.

Blaisdell, G. A., Mansour, N. N. & Reynolds, W. C. 1991 Numerical simulations of compressible homogeneous turbulence. *Tech. Rep.* No. TF-50. Thermosciences Division, Department of Mechanical Engineering, Stanford University.

Comte-Bellot, G. & Corrsin, S. 1971 Simple Eulerian time correlation of full and narrow–band velocity signals in grid-generated 'isotropic' turbulence. *J. Fluid Mech.* **48** (2), 273–337.

Ducros, F., Ferrand, V., Nicoud, F., Weber, C., Darracq, D., Gacherieu, C. & Poinsot, T. 1999 Large-eddy simulation of the shock/turbulence interaction. *J. Comput. Phys.* **152**, 517–549.

Erlebacher, G. & Hussaini, M. Y. 1998 Nonlinear strong shock interactions: a shock fitted approach. *Theor. Comput. Fluid Dyn.* **11**, 1–29.

Ghosh, S. & Mahesh, K. 2008 Numerical simulation of the fluid dynamic effects of laser energy deposition in air. *J. Fluid Mech.* **605**, 329–354.

Glumac, N., Elliott, G. & Boguszko, M. 2005 Temporal and spatial evolution of thermal structure of laser spark in air. *AIAA J.* **43** (9), 1984–1994.

Jacquin, L., Blin, E. & Geffroy, P. 1993 An experimental study on free turbulence/shock wave interaction. In *Turbulent Shear Flows 8* (ed. F. Durst, R. Friedrich, B. E. Launder, F. W. Schmidt, U. Schumann & J. H. Whitelaw), pp. 229–248. Springer.

Kandala, R. 2005 Numerical simulations of laser energy deposition for supersonic flow control. PhD thesis, Department of Aerospace Engineering and Mechanics, University of Minnesota, Minneapolis, MN.

Lee, S., Lele, S. K. & Moin, P. 1993 Direct numerical simulation of isotropic turbulence interacting with a weak shock wave. *J. Fluid Mech.* **251**, 533–562.

Lee, S., Lele, S. K. & Moin, P. 1997 Interaction of isotropic turbulence with shock waves: effect of shock strength. *J. Fluid Mech.* **340**, 225–247.

Mahesh, K., Lele, S. K. & Moin, P. 1994 The response of anisotropic turbulence to rapid homogeneous one-dimensional compression. *Phys. Fluids* **6**, 1052–1062.

Mahesh, K., Lele, S. K. & Moin, P. 1995 The interaction of an isotropic field of acoustic waves with a shock wave. *J. Fluid Mech.* **300**, 383–407.

Mahesh, K., Lele, S. K. & Moin, P. 1997 The influence of entropy fluctuations on the interaction of turbulence with a shock wave. *J. Fluid Mech.* **334**, 353–379.

Molina-Morales, P., Toyoda, K., Komurasaki, K. & Arakawa, Y. 2001 CFD simulation of a 2-kW class laser thruster. *Paper* 2001–0650. AIAA.

Riggins, D. W., Nelson, H. F. & Johnson, E. 1999 Blunt-body wave drag reduction using focused energy deposition. *AIAA J.* **37** (4), 460–467.

Rogallo, R. S. 1981 Numerical experiments in homogeneous turbulence. *Tech. Memo.* No. 81315. NASA.

Wang, T. S., Chen, Y. S., Liu, J., Myrabo, L. N. & Mead, F. B. 2001 Advanced performance modelling of experimental laser lightcrafts. *Paper* 2001–0648. AIAA.

Yee, H. C., Sandham, N. D. & Djomehri, M. J. 1999 Low-dissipative high-order shock–capturing methods using characteristic-based filter. *J. Comput. Phys.* **150**, 199–238.